CHAPTER 3 THEORY

3.1 Introduction

Colloidal liquid aphrons (CLAs) are micron-sized solvent droplets surrounded by a thin aqueous film which is stabilized by a mixture of non-ionic and ionic surfactants. They were first described by Sebba [23] in 1972, who postulated that the surfactant molecules in the aqueous film formed three distinct interfaces (a monolayer and a separate bilayer) in order to account for the stability of these solvent droplets when dispersed in a continuous aqueous medium. Recently, Deng *et al.* [24] was replaced the inner oil phase of CLAs by water-in-oil emulsion to develop a new kind of dispersion named as colloidal emulsion aphrons (CEAs). The most remarkable features of the CEAs technique for catalyst preparation are: the particles size can be controlled to a great extent, a narrow particle size distribution, the metal particles are reduced directly in the CEAs, bimetallic particles can be obtained at room temperature and no effect of support on the formation of the particles [25]. From the advantage of CEAs, CeO_2 will prepared by this technique.

General information of CeO_2 and the CEAs properties, especially the dispersibility and stability were described in this chapter. Parameters affecting the average particle size of CeO_2 will be discussed.

3.2 Cerium oxide

Cerium (IV) oxide, also known as ceric oxide, ceria, cerium oxide or cerium dioxide, is an oxide of the rare earth metal cerium. It is a pale yellow-white powder with the chemical formula CeO_2. Powdered ceria is slightly hydroscopic and will also absorb a small amount of moisture and carbon dioxide from the atmosphere. Cerium also forms cerium (III) oxide, Ce_2O_3, but CeO_2 is the most stable phase at room temperature and under atmospheric condition.

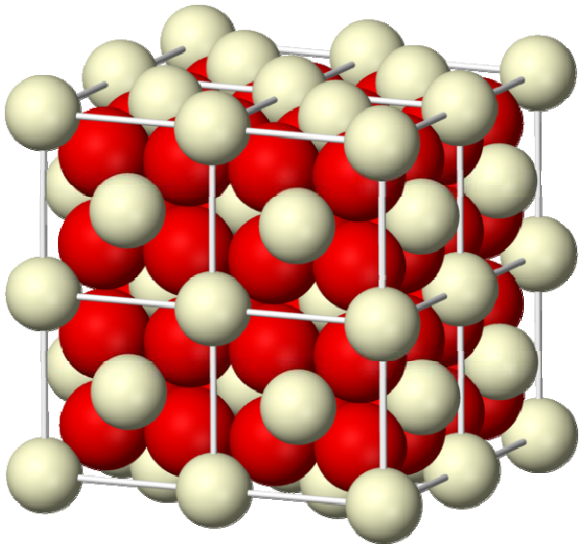

Figure 3.1 The 3D image of CeO_2 molecule [26].

Properties of Cerium oxide

Molecular formula	CeO_2
Molar mass	172.115 g/mol
Appearance	White or pale yellow solid, slightly hygroscopic
Density	7.650 g/cm^3, solid
	7.215 g/cm^3, fluorite phase
Melting point	2400°C
Boiling point	3500°C
Odor	Odorless
Soluble in water	Insoluble
Crystal structure	Cubic, face centered

3.2.1 Cerium oxide typical application [27]

1) Used in precision polishing and lapping application, especially for glass.

2) Used in the wall of self-cleaning ovens as a hydrocarbon catalyst during the high temperature cleaning process.

3) Cerium oxide is transparent for visible light, it absorbs ultraviolet radiation strongly, so it is a prospective replacement of zinc oxide and titanium dioxide in sunscreens, as it has lower photocatalytic activity. However, its thermal catalytic

properties have to be decreased by coating the particles with amorphous silica or boron nitride.

4) In the doped form, (it comes from cerium and oxygen) cerium oxide is of interest as a material for solid oxide fuel cell or SOFCs because of its relatively high oxygen ion conductivity (i.e. oxygen atoms readily move through it) at intermediate temperatures (500-800˚C). Undoped and doped ceria also exhibit high electronic conductivity at low partial pressures of oxygen due to the formation of small polarons. However, doped ceria has an extended electrolytic region (area of predominant ionic conductivity), over that of ceria, that allows its use as an electrolyte in SOFCs. Substituting a fraction of the ceria with gadolinium or samarium will introduce oxygen vacancies in the crystal without adding electric charge carriers. This increases the ionic conductivity and results in a better electrolyte.

5) Under reducing conditions, those experimented on the anode side of the fuel cell, a large amount of oxygen vacancies within the ceria electrolyte can be formed. Some of the cerium (IV) oxide is also reduced to cerium (III) oxide under these conditions which consequently increases the electronic conductivity of the material. The lattice constant of ceria increase under reducing conditions as well as with decreasing nanocrystal size in nanocrystalline ceria, as a result of the cerium cation from a +4 to a +3 state in order to charge compensate for oxygen vacancy formation.

6) Ceria has been used in catalytic converters in automotive applications. Since ceria can become non-stoichiometric in oxygen content (i.e. it can give up oxygen without decomposing) depending on its ambient partial pressure of oxygen, it can release or take in oxygen in the exhaust stream of a combustion engine. In association with other catalysts, ceria can effectively reduce NO_x emissions as well as convert harmful carbon monoxide to the less harmful carbon dioxide. Ceria is particularly interesting for catalytic conversion economically because it has been shown that adding comparatively inexpensive ceria can allow for substantial reductions in the amount of platinum needed for complete oxidation of NO_x and other harmful products of incomplete combustion.

7) Due to its fluorite structure, the oxygen atoms in a ceria crystal are all in a plane with one another, allowing for rapid diffusion as a function of the number of oxygen vacancies. As the number of vacancies increases, that ease at which oxygen can move around in the crystal increase, allowing the ceria to reduce and oxidize molecules or co-catalysts on its surface. It has been shown that the catalytic activity of ceria is

directly related to the number of oxygen vacancies in the crystal, frequently measured by using X-Ray Photoelectron Spectroscopy to compare the ratios of Ce^{3+} to Ce^{4+} in the crystal.

8) Ceria can also be used as a co-catalyst in a number of reactions, including the water-gas shift and steam reforming of ethanol or diesel fuel into hydrogen gas and carbon dioxide (with varying combinations of rhodium oxide, iron oxide, cobalt oxide, nickel oxide, platinum and gold), the Fischer-Tropsch reaction, and selected oxidation (particularly with lanthanum). In each case, it has been shown that increasing the ceria oxygen defect concentration will result in increased catalytic activity, making it very interesting as a nanocrystalline co-catalyst due to the heightened number of oxygen defects as crystallite size decreases at very small sizes, as many as 10% of the oxygen sites in the fluorite structure crystallites will be vacancies, resulting in exceptionally high diffusion rates.

3.3 Colloidal Emulsion Aphrons Method (CEAs)

3.3.1 Structure of CEAs [23, 24]

The proposed structure of colloidal emulsion aphrons was sketched in Figure 3.2 CEAs are composed of large numbers of micron-sized emulsion-cores encapsulated by soapy shell. According to Sebba's description, the soapy shell has an inner as well as an outer surface and either surface has surfactant monolayer adsorbed on it. The inner surface has oriented surfactant molecules that are hydrophilic pointing inwards and hydrophobic outwards and the outer surface has surfactant molecules that are hydrophobic outwards. If ionic surfactants are used, the hydrophobic outer surface absorbs surfactant ions from the outer aqueous phase to form diffuse electrical double layers. The soapy shell makes each aphron hydrophilic. The emulsion-core is of water-in-oil type and the inner aqueous phase is dispersed in the oil phase (membrane phase) in the form of tiny droplets. There are some common properties for CEAs and CLAs, such as high dispersibility, large surface areas and there exists soapy shell between the outer phase and dispersed phase. The main difference lies in the dispersed phase. The dispersed phase in CLAs is oil whereas it is water-in-oil emulsion in CEAs. This difference may make distinct diversities in separation ability and efficiency between them.

To some extent, CEAs are similar to ELM. When they are dispersed in bulk water (feed phase), they are all water-in-oil-in-water (W/O/W) dispersion. But there also exists distinct differences. First, the aphrons of CEAs are smaller than the globules of ELMs. The globule sizes of ELM are usually between 0.2 and 2 mm, however, the CLA aphron sizes are mainly in the range of 10–100 μm. Second, it is under stirring that the water-in-oil emulsion can disperse into outer aqueous phase (feed phase) to form $W_1/O/W_2$ liquid membrane system and the globules of W/O emulsion easily aggregate without stirring. So the separation efficiency is not ideal when ELM is applied to the extraction process without sufficient stirring, such as the treatment of drug overdose or food poisoning. To the contrary, the CEAs dispersion is already a $W_1/O/W_2$ system composed of large numbers of micron-sized aphrons isolated by very thin continuous aqueous lamella (seen in Figure 3.3). The inner aqueous phase W_1 is the tiny droplets dispersed in the oil phase of the emulsion-cores. The outer aqueous phase W_2 is the thin lamella surrounding the CEA aphrons. It is continuous phase though its volume is very small compared with that of emulsion-cores. When CEAs were added into the feed phase, they dispersed spontaneously due to the hydrophilicity of the soapy shell. At this time, the outer phase of CEAs W_2 mixed with the feed phase forming the bulk water phase. Upon the difference of CEAs from traditional $W_1/O/W_2$ double emulsions, it is similar to that of CLAs from high- internal-phase-ratio emulsions (HIPREs). A definitive structural study is needed if the structure model proposed by Sebba is to be fully confirmed. In CEAs dispersion, because it is only the special case that the oil inner phase is replaced by water-in-oil emulsion, the surface structure should be similar to that of CLAs and the soapy shell consisting of multi-layer surfactants should exist as well.

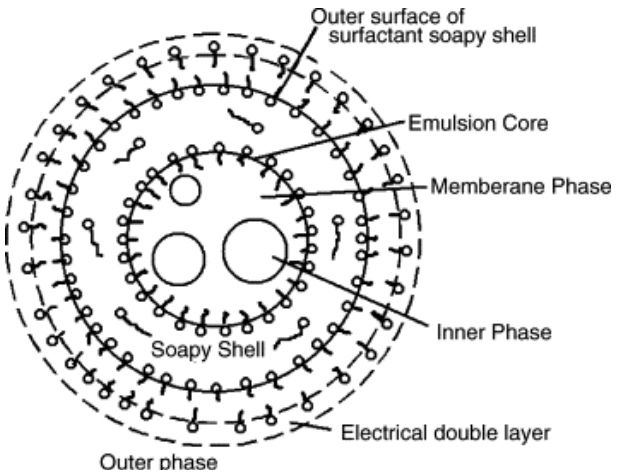

Figure 3.2 Proposed structure of CEAs [24].

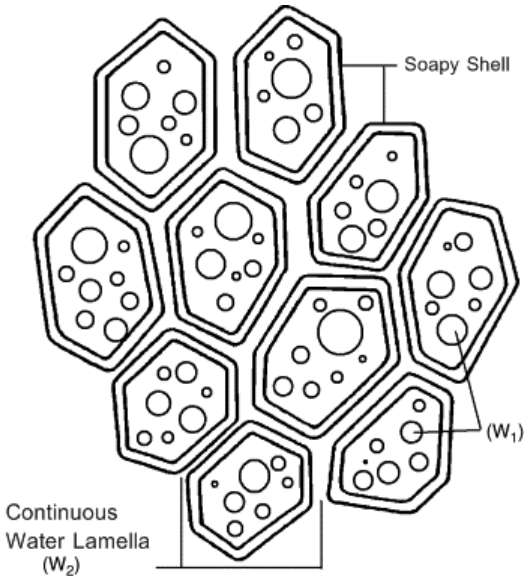

Figure 3.3 Proposed pileup state for CEAs [24].

3.3.2 Preparation of nanoparticles by CEAs [24, 28]

There are two essential steps for the preparation of CEAs: (1) the preparation of water-in-oil emulsion and (2) the formation of CEAs.

3.3.2.1 Preparation of water-in-oil emulsion

Took some quantity of cerium source aqueous solution and oil phase containing surfactant into conical flask and the flask was tightly covered to prevent losses by splashing or evaporation. The oil–water mixture was violently stirred under ultrasonic condition and the mixture formed a water-in-oil emulsion with the inner aqueous droplets of 1-5 μm in diameter. The droplets diameter scale could vary with the stirring speed, the stirring time, the time of ultrasonic action and the surfactant concentration, etc. In all the following experiments, the emulsion was prepared under the same stirring and ultrasonic conditions unless specific declaration.

3.3.2.2 Formation of CEAs

Some aqueous solution containing the hydrophilic surfactant was strongly stirred or shaken until a large amount of gas foam was formed. The water-in-oil emulsion previously prepared was gradually dropped into the foam. The foam would slowly disappear and some aphrons shaped. The emulsion was being added slowly under low-speed mixing rate until all the required volume emulsion was added and then the

colloidal emulsion aphron dispersion was formed. This dispersion prepared above could exist with no obvious phase separation for 24 h or even a week. When the PVR (ratio of the volume of hydrophilic surfactant aqueous solution to the volume of W/O emulsion) reaches 5, CEAs becomes viscous.

3.3.3 Dispersibility of CEAs [24]

The soapy shells around the CEAs aphrons qualify them for the spontaneous hydrophilicity. The CEAs can easily disperse in the water. Figure 3.4 (a) and (b) are the states when CEAs were poured into water and 3 s after, respectively. It can be seen that the turbulent motion from the dumpage was enough to make CEAs dissipate in water without extra stirring. This property brings about convenience for the extraction which is difficult to be stirred sufficiently, to the contrary, the W/O emulsion could not disperse spontaneously when it is poured into water and easily separated from water quickly (seen in Figure 3.5 (a) and (b)). Under the weak stirring, CEAs kept the dispersed state well (Figure 3.6 (a)), however the W/O emulsion was difficult to dissipate (Figure 3.6 (b)).

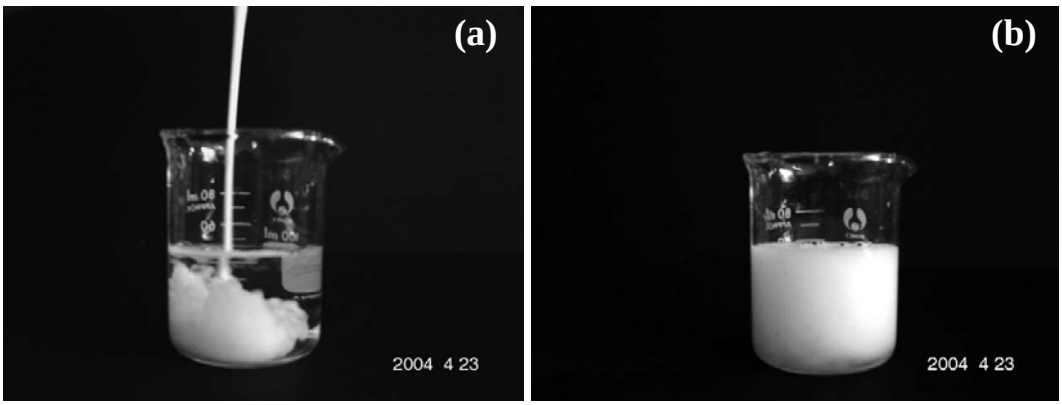

Figure 3.4 (a) The state when CEAs were being poured into water and (b) The state 3 s after CEAs were poured into water [24].

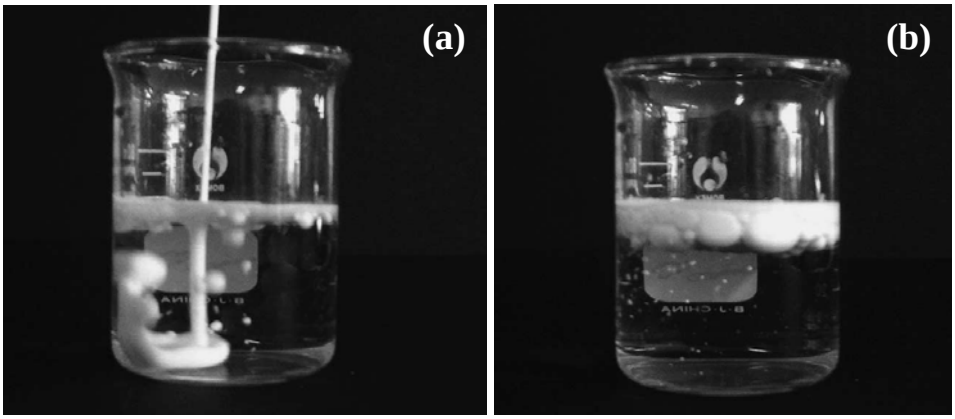

Figure 3.5 (a) The state when W/O emulsion was being poured into water and (b) The state 3 s after W/O emulsion was poured into water [24].

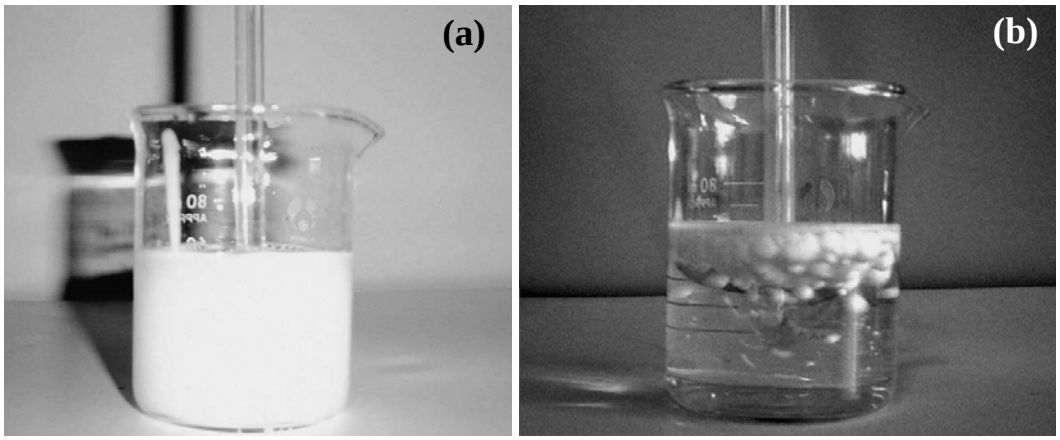

Figure 3.6 (a) The dispersion state of CEAs in water with weak stirring and (b) The state of W/O emulsion in water with weak stirring [24].

3.4 Influence of various factors on the nanoparticle size

3.4.1 Water content and the size of water droplets

The size of the final particle will much depend on the size of the droplets in the inner phase. The droplet size will be influenced by the water-to-surfactant ratio, ω. An increase of this ratio at constant concentration of surfactant will increase the average diameter of the droplets. Lisiecki and Pileni [29] reported that the size of Cu nanoparticles prepared in a system consisting of AOT, cyclohexane and water increased from 2 to 10 nm as ω changed from 1 to 10. Qiu *et al.* [30] synthesized CeF_3 nanoparticles. With increasing water content and precursor concentration, the particle

size and polydispersity rose and the morphology of the particles was converted from the mixtures of spherical and cylindrical particles to the mixtures of cylindrical and polygonal particles. When water content and Ce^{3+} concentration were below 8% and 0.2 mol/l, respectively, the CeF_3 nanoparticles with small size and good monodispersity were obtained.

3.4.2 Surfactant concentration

When the amount of water and oil is kept at fixed values, an increase of the amount of surfactant will increase the number of droplets. That means that the number of metal ions per droplet will decrease and consequently the size of the particles [25, 29]. Several studies have shown that the size of the droplets has a great influence on the size of the particles that are formed after precipitation of the precursor. However, there is not any direct correlation between the size of the droplets (10–100 nm) and the size of the obtained particles.

3.4.3 Nature of the reducing agent

Hydrazine is an efficient reducing agent for transition metal salts such as dihydrogen hexachloroplatinate. The reduction process is in this case completed instantly and is very fast in comparison to when using pure hydrogen. As a general rule, a fast nucleation process will result in the production of small particles. Furthermore, when increasing the concentration of hydrazine while the concentration of metal salt is kept constant, a decrease in the particle size is observed. Chen and Wu [31] showed when Ni particles were prepared in a microemulsion containing cetyltriammonium bromide (CTAB) as surfactant, *n*-hexanol and water. The diameter of the nickel particles decreases when the ratio of the hydrazine to nickel chloride concentrations increases. The diameter of the particles reaches a constant value when this ratio is above 10.

3.4.4 The continuous phase

The micellar dynamics is affected by changing the chain length of the oil phase. The longer the chain length of the oil, the more difficult it is to penetrate into the surfactant tail and align itself parallel to the surfactant tails. As a result, the extent of interaction between surfactant tail and the solvent chain decreases with an increase in chain length of the alkyl solvent. On the other hand, interdroplet tail-tail interaction of two surfactant

molecules increases, due to the weak presence of solvent molecules in the tail region of the droplet. The net effect results in an increase in the micellar exchange rate with an increase in the chain length of the alkyl solvent. Bagwe and Khilar [32] synthesized silver chloride nanoparticles using various organic solvent. It was found that the particles were spherical in *n*-heptane and *n*-decane while there were spherical and cubical particles in cyclohexane and in AOT/decane medium the particles formed were smaller in size and larger in number as compared in the other two systems. Kishida *et al.* [33] studied the effect of an organic solvent on Rh particle size. Alcohol with a carbon number of 2-3 was used as organic solvent. It was found that the Rh particle size increased from 3.4 to 5.0 nm as the specific permittivity of the alcohols increased.

3.4.5 The hydrophilic and hydrophobic group of surfactant

An increase of hydrophilic group chain length. It is known that the formation of water pool in the reverse micelles is occurred from the dispersion of water by the hydrophilic group of surfactant. With a decrease of hydrophilic group chain length, the formation of water pool in the reverse micelles becomes loose and then the crystallite size increases by the rapid hydrolysis of water. With an increase of hydrocarbon (hydrophobic group) chain length, the size of reverse micelles decreases because the hydrocarbon chain prohibits the access of the water near the micelles. Lee *et al.* [34] shows the crystallite size of titania particles prepared using different surfactants. When Brij series were used as surfactants, the crystallite size decreases from 17 to 10 nm with an increase of hydrophilic group chain length. When Tween series were used as surfactants, the crystallite size decreases from 12 to 9 nm with an increase of hydrocarbon (hydrophobic group) chain length. Sa-a [35] synthesized CeO_2 nanoparticles using different non-ionic surfactant. It was found that the average particle size prepared from PE4LE was smaller than from Brij96.

3.4.6 The calcination temperature

An increase of calcination temperature, the growth rate of particles increases more rapidly than the nucleation rate does, and the aggregation trend of particles becomes stronger. Therefore, the average size of particles increases with increasing of calcination temperature. He *et al.* [6] reported that the average size of CeO_2 particles increases sharply with the rise of calcination temperature and Lee *et al.* [34] shown the crystallite

size of the anatase phase of titania was increased from 7 to 21 nm as the calcination temperature increased from 300 to 600°C.

3.5 Gas sorption measurement of adsorbents

To evaluate exact such pore parameters, the most commonly used method is gas sorption measurement. The gas sorption measurement is a widely used nondestructive method to analyze pore size and distribution. Its best working rang is from micropore up to 200 nm pore width. Gas sorption measurement is one of the most applicable methods for catalysts material such as CeO_2 which are either mesoporous or microporous.

The following is a brief description of its working rationale. In an adsorption process, the amount of adsorbed gas (i.e., adsorbate) at the surface of a porous material (i.e., adsorbent) depends on its microstructure, pressure and temperature [36]. Therefore, the pore structure of the adsorbent can be quantitatively evaluated from the gas sorption isotherm. The gas sorption isolate is a plot of the amount of adsorbed gas as a function of as pressure at a constant temperature, usually liquid nitrogen temperature (77 K). The pressure is expressed as relative pressure, a function of saturated pressure. The amount of the adsorbed gas is expressed in volume at standard temperature and pressure (STP) relative to the weight of the sample. During the measurement, the pressure of gas increases from vacuum to saturation pressure, and the gradually decreases back to vacuum. Along with the pressure variation, two branches of the isotherm are obtained, namely adsorption branch and desorption branch. The specific surface areas were calculated using Brunauer-Emmett-Teller (BET) equation [37] as shown in the following equation:

$$\frac{P}{V(P_0 - P)} = \frac{1}{V_m C} + \frac{(C-1)P}{CV_m P_0} \tag{3.1}$$

Where V (cm^3) is volume of N_2 adsorbed on adsorbent surface, V_m (cm^3) is volume of N_2 adsorbed when the entire adsorbent surface is covered with a complete unimolecular layer, P, P_0 (mmHg) is vapor and saturated pressure, respectively and C is the constant specified by each gas. C is shown in this equation:

$$C = \exp[\frac{\Delta H_A - \Delta H_L}{RT}] \quad (3.2)$$

Where ΔH_A is the heat of adsorption and ΔH_L is the heat of liquefaction.

V_m obtained from the straight line of equation 3.1 is used to calculate surface areas, S (m^2) from equation 3.3:

$$S = \frac{V_m N_{AV}}{22400} a_m \quad (3.3)$$

Where N_{AV} is Avogadro number (6.02×10^{23}) and a_m is the projection area per molecule (0.162 nm^2/molecule)

Micropore volume and mesopore surface area were evaluated using *t*-plot method. This is the plot of the volume of N_2 adsorbed versus the statistical adsorbed film thickness, *t* (A) calculated from Halsey equation [38] as shown in equation 3.4.

$$t = 3.54 \left[\frac{5}{2.3031 \log(\frac{P_0}{P})}\right]^{\frac{1}{3}} \quad (3.4)$$

Mesopore surface area is calculated from equation 3.5 where V/t is the slope of line A. The slope of line B refers to the total surface area. Micropore volume (V_m) is obtained from the y-intercept of line A and calculated using equation 3.6.

$$S = \frac{V(15.47)}{t} \quad (3.5)$$

$$V_{mi} = 0.001547\, i \quad (3.6)$$

Where *i* is y-intercept of line A.

3.5.1 Classification of Adsorption Isotherm [39]

Depending on the relation strength of the interactions among adsorbate molecules and the structure of the adsorbent, the adsorbate-adsorbent system may exhibit monolayer adsorption, multilayer adsorption, capillary condensation or a combination. The shape of an isotherm indicates the occurrence of these phenomena, and furthermore, reveals the porosity of the adsorbent. According to the IUPAC classification, the majority of the adsorption isotherms may be categorized into six types as shown in Figure 3.7.

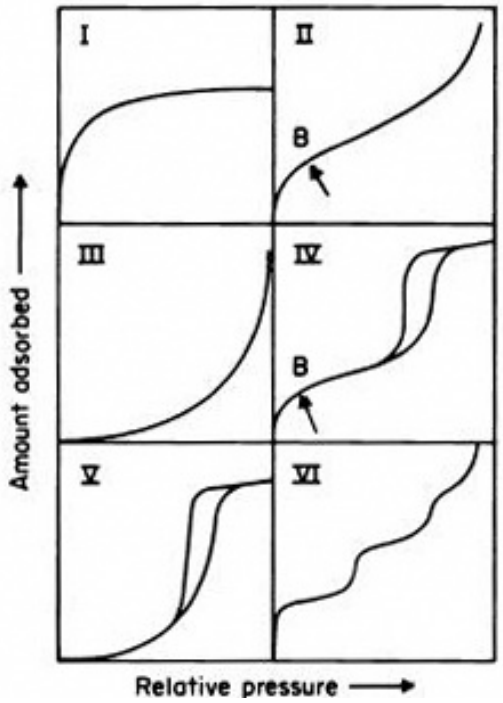

Figure 3.7 IUPAC classification of physisorption isotherm [39].

Type I reversible isotherms are typical in microporous solids with relatively small external surfaces. Monolayer adsorption occurs significantly at relatively low partial pressures < 0.5 P/P_0.

Type II reversible isotherms describe the gas sorption with a non-porous or macroporous solid in which multi-layer adsorption forms due to a strong interaction between adsorbed molecules.

Type III reversible isotherms are convex towards the relative pressure axis. This type of isotherm originates from both non-porous and microporous solid. These isotherms are characteristic of weak adsorbate-adsorbent interactions.

Type IV isotherm exhibits a plateau with a characteristic hysteresis loop. The presence of hysteresis loops is associated with mesoporous solid, where capillary condensation occurs.

Type V isotherms are related to the Type III isotherms in that the adsorbate-adsorbent interactions are weak. Type V isotherms are usually obtained from microporous or mesoporous solids.

Type VI isotherms are stepwise, which represent multilayer adsorption on a uniform non-porous surface.

Regarding to the Type IV adsorption isotherm, the hysteresis loops may exhibit a variety of shapes and sizes, which are affected by pore shape, size of the network and degree of interconnection. Classified by IUPAC, there are four typical types of isotherms with hysteresis loop, which are shown in Figure 3.8.

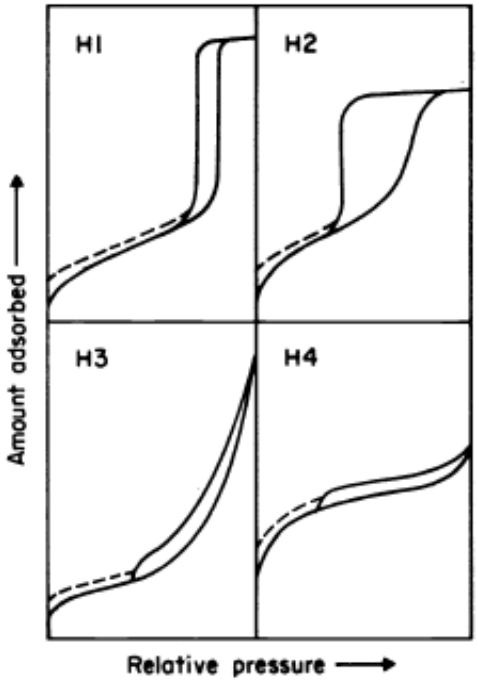

Figure 3.8 IUPAC classification of hysteresis loops [39].

Type H1 loop is often associated with pores with regular shape and narrow size distribution.

Type H2 loop used to be attributed to link-bottle pores, which have narrow necks and wide body. Now it has been well recognized that network effect also play an important role in the loop formation.

Type H3 loop is observed with aggregates of plate-like particle giving rise to slit shape pores.

Type H4 loop is usually associated with narrow slit-like pores.

The observed hysteresis may be the result of two basic mechanisms, namely, “single pore mechanism” and “network mechanism”. In “single pore mechanism”, a metastable phase may persist beyond the vapor-liquid coexistence pressure during the adsorption and desorption processes where a vapor phase may be present at pressure above the condensation pressure, and a liquid phase below the condensation pressure.

The second mechanism is related to the topology of the pore network. During the adsorption process, the vapor needed to fill the pore can be transported either through the liquid or through the vapor phases. However, during the desorption process, the desorbed vapors must be transported to outside only through the vapor phase. Vaporization therefore occurs only in pores connected to the bulk vapor phase, not in pores surrounded by other liquid filled pores. Once vaporization has occurred with the vapor phase, and will vaporize when it is thermodynamically favorable. As a result, clusters of vapor-filled pores grow from the surface until enough pores are opened.

3.6 Methane steam reforming [15, 17, 22, 40-47]

The methane steam reforming is a widely practiced technology for production of hydrogen or synthesis gas for later utilization in fuel cells. Three main reactions are always carried out as presented in the following equations:

$$CH_4 + H_2O \leftrightarrow CO + 3H_2 \quad (3.7)$$

$$CO + H_2O \leftrightarrow CO_2 + H_2 \quad (3.8)$$

$$CH_4 + 2H_2O \leftrightarrow CO_2 + 4H_2 \quad (3.9)$$

Both water–gas shift reaction (Eq. (3.8)) and reverse methanation (Eq. (3.9)) are associated with the steam reforming over a catalyst at elevated temperatures. The reverse methanation (Eq. (3.9)) is thermodynamically linearly dependent on methane steam reforming and water–gas shift reaction, but it is kinetically independent. Due to the overall high endothermic nature of the reactions, they are carried out at high temperature (700-900°C). In recent years, many researchers have also investigated the

addition of oxygen together with methane and steam in a single process, calling an autothermal reforming. This reaction is an economical process, in which the steam reforming of methane (Eq. (3.7)) is combined with the partial oxidation of methane, as presented in the following equation:

$$CH_4 + ½O_2 \quad \leftrightarrow \quad CO + 2H_2 \tag{3.10}$$

By this combination, exothermic heat from the partial oxidation can directly supply the energy required for the endothermic steam reforming reaction. Therefore, it is considered to be thermally self-sustaining and consequently more attractive than the steam reforming. However, the main disadvantage of this reaction is the lower production of synthesis gas (H_2 and CO) from this reaction compared to the steam reforming. Currently, the commercial process for the production of hydrogen and synthesis gas is still based on the steam reforming reaction using nickel catalyst on supports such as Al_2O_3, MgO, $MgAl_2O_4$ or their mixtures. Worldwide efforts are in progress to develop a novel catalyst with higher activity and stability for the reforming reactions. Various precious metals such as Pt, Rh, and Ru have been reported to be active for the reforming reactions and resistant to the carbon formation [17, 40, 41]. However, the current prices of these metals are very high for commercial uses, and the availability of some precious metals such as ruthenium was too low to have a major impact on the total reforming catalyst market.

Selection of a support material is another important issue as there was some evidence that metal catalysts are not very active for the steam reforming when supported on inert oxides [42]. Various supports have been investigated, for example, α-Al_2O_3, γ-Al_2O_3, and γ-Al_2O_3 [22] with alkali metal oxide and rare earth metal oxide, $CaAl_2O_4$ and CeO_2-ZrO_2 [15]. A promising catalyst system for the reforming reactions appeared to be a metal on CeO_2-ZrO_2 support, where the metal can be Ni, Pt or Pd [43, 44]. Ni/CeO_2-ZrO_2 has been successfully applied to the partial oxidation and the autothermal reforming of methane. It is well established that ceria and metal oxide (e.g. Gd, Nb, and Zr) doped cerias provide high oxygen storage capacity, which is beneficial in oxidation processes. Moreover, it has been reported that the gas–solid reaction between CeO_2 and CH_4 produces synthesis gas with a H_2/CO ratio of two, while the reduced ceria, CeO_{2-n},

can react with CO_2 and H_2O to produce CO and H_2, respectively, according to the following reactions:

$$CeO_2 + nCH_4 \rightarrow CeO_{2-n} + nCO + 2nH_2 \quad (3.11)$$

$$CeO_{2-n} + CO_2 \leftrightarrow CeO_2 + CO \quad (3.12)$$

$$CeO_{2-n} + H_2O \leftrightarrow CeO_2 + H_2 \quad (3.13)$$

The addition of zirconium oxide (ZrO_2) to cerium oxide (CeO_2) has been reported to improve the oxygen storage capacity, redox property, thermal stability and catalytic activity. This high oxygen storage capacity was associated with enhanced reducibility of cerium(IV) in CeO_2–ZrO_2, which is a consequence of the high O^{2-} mobility inside the fluorite lattice. One possible reason for the increasing mobility might be related to the lattice strain, which is generated by the introduction of a smaller isovalent Zr cation into the CeO_2 lattice (Zr^{4+} has a crystal ionic radius of 0.84 Å, which is smaller than 0.97 Å for Ce^{4+} in the same co-ordination environment). Due to the high thermal stability of this material, CeO_2–ZrO_2 would be a good candidate to be used as the catalyst support for high temperature steam reforming reactions.

For the steam reforming of methane over Ni/Ce–ZrO_2, in addition to the reactions on Ni surface, the redox reaction between inlet CH_4 and the lattice oxygen (O_x) on CeO_2–ZrO_2 surface also takes place, producing H_2 and CO (Eq. (3.11)). Moreover, the reduced CeO_2–ZrO_2 can react with inlet H_2O to produce more H_2 and to recover O_x. The proposed mechanism for these redox reactions, involving the reactions between methane and/or an intermediate surface hydrocarbon species with the lattice oxygen (O_x) on CeO_2–ZrO_2 surface and the recovery of O_x by steam [17], is presented schematically below:

$$CH_4 + 2S \leftrightarrow CH_3\text{-}S + H\text{-}S \quad (3.14)$$

$$CH_3\text{-}S + S \leftrightarrow CH_2\text{-}S + H\text{-}S \quad (3.15)$$

$$CH_2\text{-}S + S \leftrightarrow CH\text{-}S + H\text{-}S \quad (3.16)$$

$$CH\text{-}S + S \leftrightarrow C\text{-}S + H\text{-}S \quad (3.17)$$

$$C\text{-}S + O_x \leftrightarrow CO + O_{x-1} + S \quad (3.18)$$

$$CO + O_x \leftrightarrow CO_2 + O_{x-1} \quad (3.19)$$

$$2H\text{-}S \leftrightarrow H_2 + 2S \quad (3.20)$$

$$H_2O + O_{x-1} \leftrightarrow O_x + H_2 \quad (3.21)$$

The surface site (S) can be either a unique site, or it can also be considered to be the same site as the catalyst oxidized site (O_x). It has been reported [17, 46] that the controlling step of these redox reactions is the reaction of methane on the CeO_2–ZrO_2 surface; in addition, the lattice oxygen is replenished by a significant rapid surface reaction of the reduced state CeO_2–ZrO_2 with H_2O.

According to the possible formation of carbon species on the surface of catalyst during the steam reforming process, the following reactions are theoretically the most probable reactions that could lead to carbon formation:

$$2CO \leftrightarrow CO_2 + C \quad (3.22)$$
$$CH_4 \leftrightarrow 2H_2 + C \quad (3.23)$$
$$CO + H_2 \leftrightarrow H_2O + C \quad (3.24)$$
$$CO_2 + 2H_2 \leftrightarrow 2H_2O + C \quad (3.25)$$

C is the carbonaceous deposits. Reactions (3.24) and (3.25) are favorable at low temperature, while reaction (3.22) is thermodynamically unflavored [46]. At such a high temperature, the Boudouard reaction (Eq. (3.22)) and the decomposition of methane (Eq. (3.23)) are the major pathways for carbon formation, as they show the largest change in Gibbs energy [47].